Article

Object-Oriented Open-Pit Mine Mapping Using Gaofen-2 Satellite Image and Convolutional Neural Network, for the Yuzhou City, China

Tao Chen [1],* , **Naixun Hu [1]**, **Ruiqing Niu [1]**, **Na Zhen [2]** and **Antonio Plaza [3]**

[1] Institute of Geophysics and Geomatics, China University of Geosciences, Wuhan 430074, China; hnx0908@cug.edu.cn (N.H.); niuruiqing@cug.edu.cn (R.N.)

[2] Geological Environment Monitoring Institute of Henan Province, Zhengzhou 450006, China; hjyzn2019@163.com

[3] Hyperspectral Computing Laboratory, Department of Technology of Computers and Communications, Escuela Politécnica, University of Extremadura, 10071 Cáceres, Spain; aplaza@unex.es

* Correspondence: taochen@cug.edu.cn

check for updates

Abstract: Our society's growing need for mineral resources brings with it the associated risk of degrading our natural environment as well as impacting on neighboring communities. To better manage this risk, especially for open-pit mine (OM) operations, new earth observation tools are required for more accurate baseline mapping and subsequent monitoring. The purpose of this paper is to propose an object-oriented open-pit mine mapping (OOMM) framework from Gaofen-2 (GF-2) high-spatial resolution satellite image (HSRSI), based on convolutional neural networks (CNNs). To better present the different land use categories (LUCs) in the OM area, a minimum heterogeneity criterion-based multi-scale segmentation method was used, while a mean area ratio method was applied to optimize the segmentation scale of each LUC. After image segmentation, three object-feature domains were obtained based on the GF-2 HSRSI: spectral, texture, and geometric features. Then, the gradient boosting decision tree and Pearson correlation coefficient were used as an object feature information reduction (FIR) method to recognize the distinguishing feature that describe open-pit mines (OMs). Finally, the CNN was used by combing the significant features to map the OM. In total, 105 OM sites were extracted from the interpretation of GF-2 HSRSIs and the boundary of each OM was validated by field work and used as inputs to evaluate the open-pit mine mapping (OMM) accuracy. The results revealed that: (1) the FIR tool made a positive impact on effective OMM; (2) by splitting the segmented objects into two groups, training and testing sets which are composed of 70% of the objects, and validation sets which are formed by the remaining 30% of the objects, then combing the selected feature subsets for training to achieve an overall accuracy (*OA*) of 90.13% and a Kappa coefficient (*KC*) of 0.88 of the whole datasets; (3) comparing the results of the state-of-the-art method, support vector machine (SVM), in OMM, the proposed framework outperformed SVM by more than 7.28% in *OA*, 8.64% in *KC*, 6.15% in producer accuracy of OM and by 9.31% in user accuracy of OM. To the best of our knowledge, it is the first time that OM information has been used through the integration of multiscale segmentation of HSRSI with the CNN to get OMM results. The proposed framework can not only provide reliable technical support for the scientific management and environmental monitoring of open pit mining areas, but also be of wide generality and be applicable to other kinds of land use mapping in mining areas using HSR images.

Keywords: open-pit mine; object-oriented methods; convolutional neural networks (CNNs); Gaofen-2; mineral resources

1. Introduction

Open-pit mining can damage the natural environment, and is prone to cause water pollution, air pollution, solid waste pollution, and geological disasters [1–5]. Mine environmental monitoring, mainly open-pit mine (OM) monitoring, has always been the top priority of mine governance and reclamation. Currently, China is speeding up green mine construction and strengthening the mine area ecological protection. Obtaining detailed information of OM is essential for the national project.

Traditional remote sensing methods addressing OM problems were mainly based on combining visual interpretation and field surveys. The results provided by the analysts are commonly subjective, time-consuming, and costly, even if the results are reliable [6]. Nowadays, with the development of high spatial resolution satellite imagery (HSRSI) and machine learning methods, many researchers have applied machine learning methods to classify the land cover in OM areas [7–9] and most of the algorithms are pixel-based [10–15].

Although the pixel-based open-pit mine mapping (OMM) approaches have achieved satisfactory OMM results, they usually ignore geometric and contextual information in multi-source image data, especially by using HSRSI [16]. Recently, some researchers have applied object-oriented methods where the units are objects of image, which are composed of pixels with similar spectral characteristics, to map the OM area [17–20]. Effective object-oriented open-pit mine mapping (OOMM) needs to define object-features from remote sensing and thematic data, e.g., information of image band, texture, and geometric features, and the number ranges from several to dozens. Nonetheless, for feature selection, there is no general rule that will affect the OOMM accuracy. When many features are available, it is a complicated process to extract appropriate features for different research areas, and a variety of OOMM methods can also be utilized [21].

Recently, one of the newest hot topics in machine learning and pattern recognition is deep learning. In deep learning, the most discriminative and representative features can be hierarchically learnt in end-to-end fashion [22]. This breakthrough was due to the interest in modeling advanced feature representations using multilayer neural networks without the need to manually design features or rules. A popular deep learning method, convolutional neural networks (CNNs), has achieved the latest results in multiple fields, e.g., visual recognition [23], image retrieval [24], and scene annotation [25]. Due to its advantages in advanced scene understanding and feature representation, CNN shows great potential in several remote sensing tasks, such as vehicle detection [26,27], road network extraction [28], remotely sensed scene classification [25,29], and semantic segmentation [30].

In this paper, a new effective OOMM framework for Gaofen-2 (GF-2) HSRSI based on CNNs is proposed. First, a multi-scale segmentation (MSS) method is used to extract three object-feature domains from the GF-2 HSRSI: spectral, texture, and geometric features. Then, gradient boosting decision tree (GBDT) and the Pearson correlation coefficient are used as an object feature information reduction (FIR) tool to recognize the important features that describe OMs. Finally, the CNN was used by combing the significant features to map the OM, and the mapping results were compared with that of the support vector machine. In total, 105 OM sites were extracted from the interpretation of GF-2 HSRSI and the boundary of each OM was validated by field work and used as inputs to evaluate the OMM accuracy. This research aims to explore the applicability of FIR methods and CNN algorithm under an object-oriented framework for OMM using 'GF-2' HSRSI.

The remainder of the paper is organized as follows: Section 2 describes the study area, the data used in this study, and introduces the detailed OOMM framework; Section 3 presents the experimental results; discussions are given in Section 4, followed by conclusions in the last section.

2. Materials and Methods

2.1. Study Area

The study area is located in the north of Yuzhou City, Henan Province, between 113.375°E to 113.561°E and 34.256°N to 34.352°N with an area of 102.59 km^2 (Figure 1). The terrain types in this area

are mainly mountains and hills. The elevation of this area ranges from 128 to 779 m with an average of 454 m. The area has a warm temperate monsoon climate in the north, with four distinct seasons. The study area is sited in the transitional zone between the Yudong Plain and the Funiu Mountain Range. It is Songying platform uprise, with Baisha and Yuzhou city syncline, Huishan, Fenghouling anticline, and Jiaozishan anticline. Yuzhou City is rich in mineral resources, while the main mineral deposits are coal, bauxite, iron, ceramic clay, limestone, sulfur, and so on, and most of them are open-pit mining. Due to many mountains and hills, rich precipitation, and open-pit mining activities, it may cause a lot of problems to the environment, which conflicts with the green mining policy of the Chinese government. The mapping of the OM is necessary for strengthening the ecological construction of mines in the future studies and government decision makers.
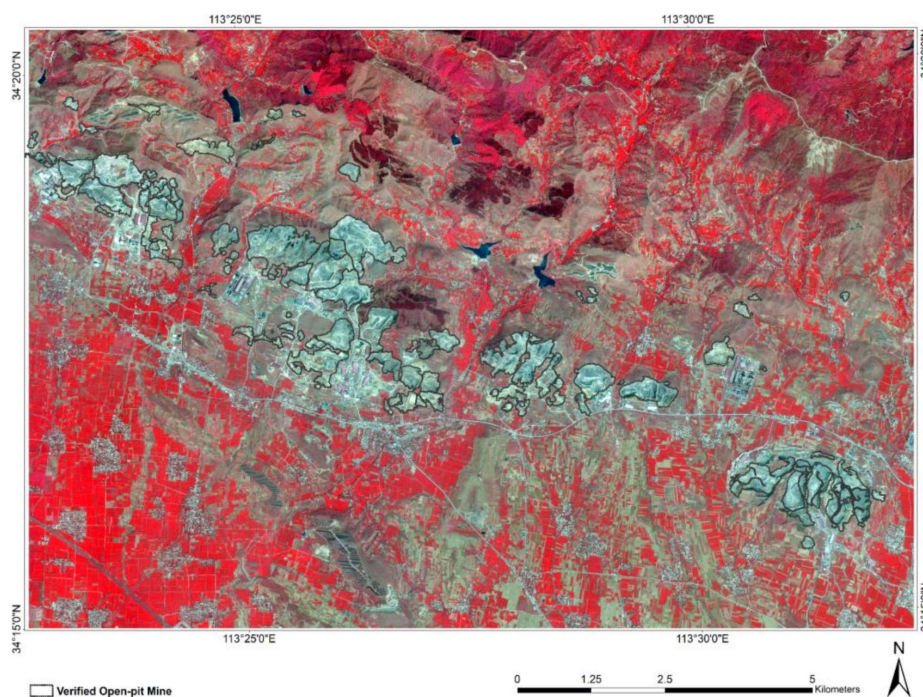

Figure 1. Location of study area (R: Band4, G: Band3, B: Band2 of GF-2 image).

2.2. Data Sources

A GF-2 HSRSI captured on 16/04/2018 was employed in this study, which has four multispectral bands (Red, Green, Blue, and Near Infrared) with a spatial resolution of 4 m. Land use categories (LUCs) of the study area were classified into seven dominating groups, including OM, waste-dump area (WDA), buildings (BUI), vegetation (VEG), road (ROA), water (WAT), and bare soil (BAS), according to the land use map provided by the Geological Environmental Monitoring Institute of Henan Province.

OM areas in this study area were visually identified on GF-2 images. Then, a series of field surveys were carried out from 27 August to 26 September 2018, with the help of Geological Environmental Monitoring Institute of Henan Province. After the field surveys, 105 Oms, which covered a total area of 9.36 km² were mapped, accounting for 9.12% of the area of the study area. The largest area of OM is 0.65 km² while the smallest is 1161 m². Finally, all the mapped OMs were subsequently digitized and rasterized into the same resolution (4 × 4 m) as the HSRSI used for the study in Environmental Systems Research Institute's ArcGIS software (Version 10.3.0). Figure 2 shows the open-pit visual interpretation key and field photo of the field work in the study area of this paper.
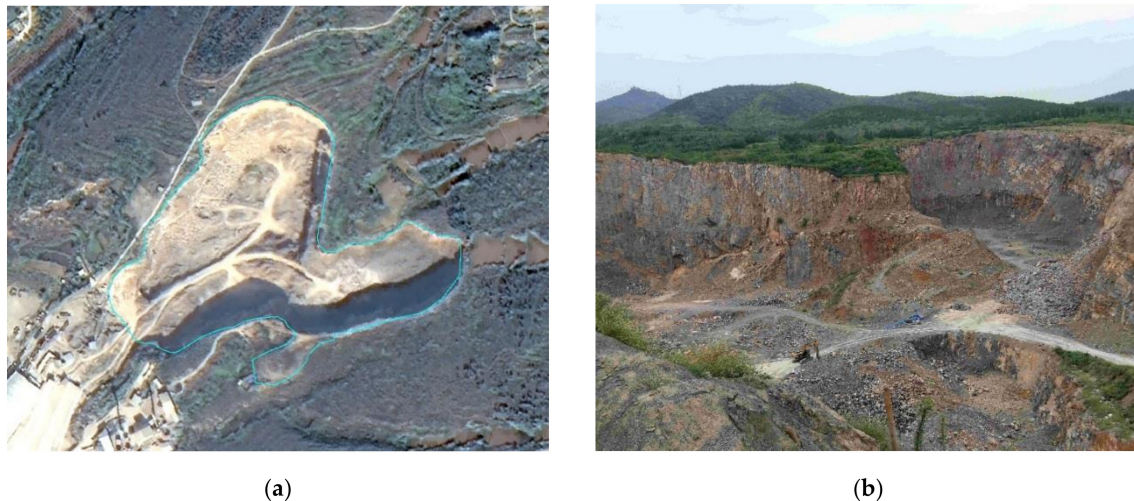
(**a**)   (**b**)

Figure 2. Visual interpretation key and field photo of open-pit mine. (**a**) Visual interpretation key of open-pit mine; (**b**) field photo of open-pit mine.

2.3. Methodology

The proposed OOMM framework (see Figure 3) is composed of three steps: image segmentation, feature selection, and open-pit mine mapping. In the first step, image objects were obtained from GF-2 HSRSI by using the MSS method based on an optimal segmentation scale selection algorithm. Then, a sample set was created, and the objects in the sample set were labeled by using the centroid inclusion principle, in which their centroids belong to a certain LUC, by combing the objects with the existing OMs and land use vectors.

In the second step, a FIR method based on the GBDT and Pearson correlation coefficient was utilized to reduce the feature sample data size. The importance of features was computed, and the features with the least importance values were dropped. Then, the relationship among these remaining features were analyzed and the most relevant features were used in the OMM procedure.

In the final OMM progress, after reducing the feature sets, two thirds of the objects were assigned as training and testing sets (TTS) and the remaining one third as validation sets (VS). Then, a CNN model was applied to classify the study area, and finally, the accuracies of classification were assessed.

2.3.1. Image Segmentation

For object-oriented methods, the necessary and first pre-condition is image segmentation, because the contour quality (such as shape and size) of the target object directly affects the subsequent image classification accuracy [31]. There are several segmentation approaches, but multi-scale segmentation (MSS), which can overcome the limitation that a single segmentation scale cannot, by extracting all types of the target object and considering the characteristics of multiple layers and multiple patterns on the actual surface [32], is selected in this study.

A bottom-up region-merging technique is used to form an object in the MSS procedure, where the smallest object contains one pixel. Based on the chosen scale (ScP), shape (ShP), and color (CP) parameters, which define the growth in heterogeneity between adjacent image objects, smaller image objects are merged into larger ones. It is known that a larger ScP leads to a larger image object, which may cause over-segmentation, while a smaller ScP results in a small size image object, which may lead to under-segmentation [33,34]. ScP is an abstract term that determines the maximum allowable heterogeneity in the resulting image object [35]. The other two important parameters are CP (representing the uniformity of the spectrum) and ShP (used to define the texture uniformity of the resulting image object). The weights of CP and ShP range from 0 to 1 and their weights are sum to 1 in the eCognition® software (Version 9.0.1). ShP is generally split into two categories: smoothness, which is employed to optimize resulting image objects by considering the smoothness of their borders

within the ShP; and compactness, which is employed to optimize the resulting image objects in regard to the overall compactness within the ShP. Besides these three parameters, we have to set a threshold *t* for the bottom-up merge process. The increase in heterogeneity has been calculated before fusing two adjacent objects. If the result goes beyond the threshold *t*, the segmentation stops.
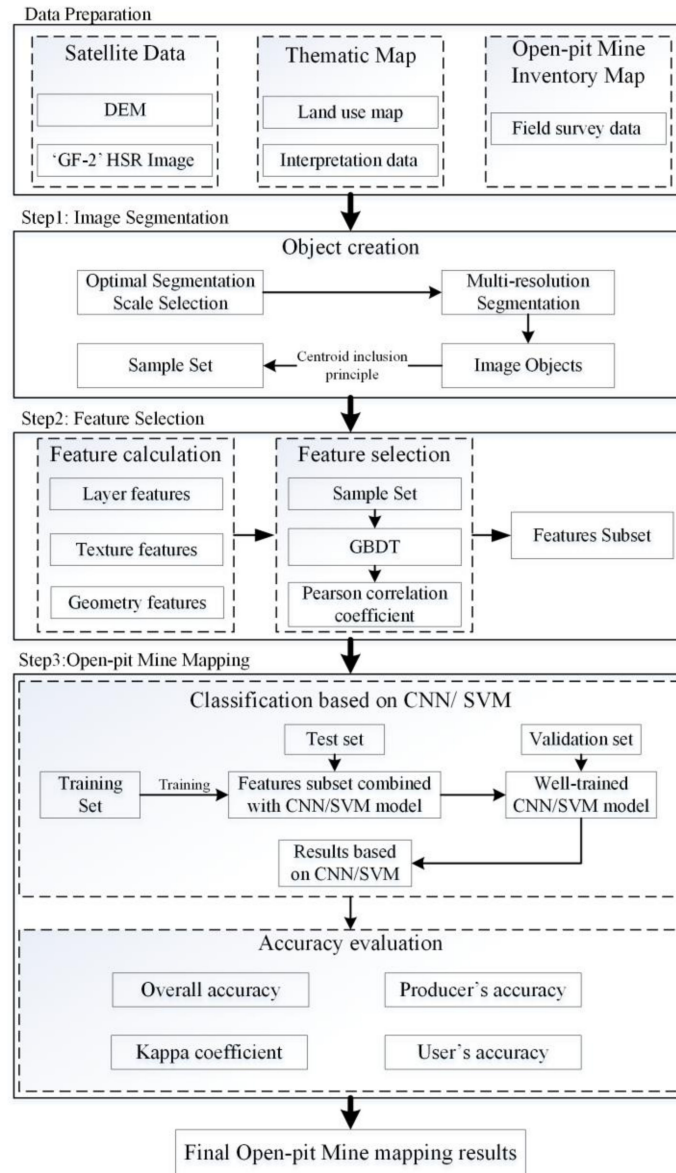

Figure 3. Flowchart of the proposed open-pit mine mapping framework.

In order to obtain good segmentation results, the segmented image objects can completely represent the contour information of a target ground object, and at the same time, the interior of the target ground object will not be segmented too "fragmented". The optimal segmentation scale of the object is calculated. In this study, a mean area ratio (MAR) method was used to calculate the best ScP by using Equation (1). This method usually selects several targets in a certain type of ground objects to replace all the ground objects of the type, and then calculates the MAR of each type according to the Equation (1) to determine the optimal segmentation scale.

$$R = \frac{1}{m} \sum_{i=1}^{m} \frac{S_{T_i}}{\sqrt{n_i} S_{O_i}}, \tag{1}$$

where R is the mean area ratio, m is the total number of LUC of the same type in the entire image, n_i is the number of objects generated by the i-th target feature segmentation, and its value is greater than or equal to 1, S_{Ti} indicates the actual area of the i-th target LUC while S_{Oi} is the total area of the i-th garget objects generated by the image segmentation.

2.3.2. Object Features Calculation

In this study, a total of 58 features, which was composed of three object-feature domains (OFDs), which were layer features (LFs), texture features (TFs), and geometry features (GFs) were extracted from the GF-2 HSRSI by utilizing the eCognition® software (Version 9.0.1) (see Table 1) [36,37].

Table 1. Object features employed in this research. OFDs: object-feature domains; LFs: layer features; TFs: texture features; GFs: geometry features.

OFDs (No.)	Features Names
LFs (32)	*Stdv*_(1,2,3,4), *Mean*_(1,2,3,4), *Ratio*_(1,2,3,4), *Brightness*, *MaxDiff*, Shadow vegetation index, Normalized difference vegetation index, Normalized difference water index, Soil brightness index, Soil adjust vegetation index, Ratio vegetation index, Mean Diff. to Neighbors_(1,2,3,4), Mean Diff. to brighter Neighbors_(1,2,3,4), Mean Diff. to darker Neighbors_(1,2,3,4)
TFs (12)	$GLCM_{\text{all dir.}}$ (Angular second moment, Entropy, Stdv, Contrast, Dissimilarity, Homogeneity, Mean, Correlation) $GLDV_{\text{all dir.}}$ (Angular second moment, Entropy, Contrast, Mean)
GFs (14)	Area, Border length, Border index, Length, Width, Length-width ratio, Shape index, Roundness, Elliptic fit, Rectangular fit, Compactness, Main direction, Asymmetry, Density

The *stdv* value is the standard deviation of all pixels' intensity values that form an image object. The *Ratio* value is the average value of the image object layer divided by the sum of the average value of all layers. The *MaxDiff* value is the absolute value of the difference between the maximum object average value ($max(\overline{O}_{i(v)})$) and the minimum object average value ($min(\overline{O}_{i(v)})$) in each layer, divided by the object brightness B, which is defined as the sum of the object averages in the same layer ($\overline{O}_{i(v)}$) divided by the corresponding number of layers (n_v).

$$MaxDiff = \frac{\left| max(\overline{O}_{i(v)}) - min(\overline{O}_{i(v)}) \right|}{B}, \tag{2}$$

$$B = \frac{1}{n_v} \sum_{i=1}^{n_v} (\overline{O}_{i(v)}). \tag{3}$$

Shadow vegetation index (SVI), normalized difference vegetation index (NDVI), normalized difference water index (NDWI), soil brightness index (SBI), soil adjust vegetation index (SAVI), and ratio vegetation index (RVI), is calculated by using Equations (4)–(9):

$$SVI = NDVI \times \rho_{NIR}, \tag{4}$$

$$NDVI = \frac{\rho_{NIR} - \rho_R}{\rho_{NIR} + \rho_R}, \tag{5}$$

$$NDWI = \frac{\rho_G - \rho_{NIR}}{\rho_G + \rho_{NIR}}, \tag{6}$$

$$SBI = \sqrt{\left(\rho_R^2 + \rho_G^2 + \rho_{NIR}^2\right)/3}, \tag{7}$$

$$\text{SAVI} = \frac{\rho_{NIR} - \rho_R}{\rho_{NIR} + \rho_R + L}(1 + L), \tag{8}$$

$$\text{RVI} = \frac{\rho_{NIR}}{\rho_R}, \tag{9}$$

where ρ_{NIR}, ρ_R, ρ_G is the reflectance of near-infrared, red, and green band, respectively.

Mean Diff. to Neighbors is the mean difference between the feature value of an image object and its neighbors of a selected class. Mean Diff. to brighter/lower neighbors is the mean difference between the feature value of an image object and the feature values of its neighbors of a selected class, which have brighter/lower values than the image object itself.

The gray level co-occurrence matrix (*GLCM*) and gray level co-occurrence vector (*GLCV*) formed the texture features in this study. Eight- and four-connected textures were calculated from *GLCM* and *GLCV*, respectively [38]. In this research, we calculated only the grey-level's co-occurrence frequencies for all directions of neighboring pixels in symmetric matrices, and a sum of all directional *GLCMs* (*GLCM*$_{\text{all dir}}$.) and *GLCVs* (*GLCV*$_{\text{all dir}}$.) were used to directly calculate eight and four rotation-invariant texture measures of each band per image object using eCognition® software [39].

The geometrical features used in this study were area, border length, border index, length, width, length-width ratio, shape index, roundness, elliptic fit, rectangular fit, compactness, main direction, asymmetry, and density. The border length of an image object is defined as the sum of the image object edges shared with other image objects or located at the edge of the entire scene. The border index feature is calculated as the ratio between the border lengths of the image object and the smallest enclosing rectangle. The length-width ratio is the ratio of length and width of an object. The shape index is calculated by dividing the boundary length feature of the image object by four times the square root of its area. The roundness feature is calculated by the difference of the enclosing ellipse and the enclosed ellipse. The calculation of elliptic fit is based on an ellipse with the same area as the selected image object. The calculation of the rectangular fit feature is based on a rectangle with the same area as the image object. The compactness feature of an image object is the product of the length and the width, divided by the number of pixels. The definition of the main direction feature of an image object is the direction of the eigenvector that belongs to the larger of the two eigenvalues. The asymmetry feature describes the relative length of an image object, compared to a regular polygon. The density feature is calculated by dividing the number of pixels forming the image object by its approximate radius according to the covariance matrix.

2.3.3. Feature Selection

Large feature sets may cause numerous problems in the classification process, such as inefficiency due to the large number of resources [40], the accuracy loss when the feature number is significantly larger than the optimal feature number [41], and unrelated inputs features that may cause the model to over-fit. Thus, eliminating the redundancy or relevance of features in the input layer is very crucial to improve the classification accuracy of a specific research area.

In this study, the GBDT based on the LightGBM library in Python language was used to calculate the importance value of each feature [42,43]. The GBDT method is a combination of decision tree and ensemble learning techniques and was designed to improve the performance of a single predictive model by combining many models [44]. It is a linear training process that trains multiple trees in series. Each tree in the model learns the classification results and residuals of all previous trees. The final result is a weighted accumulation of the node values of all decision trees. Then, the importance values of all features are normalized and are converted into importance percentages. The features with an importance value of 0 indicate that they have no contribution to the classification prediction process and need to be removed. In addition, according to specific research needs and accuracy requirements, the cumulative importance threshold can be artificially set by using the trial-and-error method, and the features beyond the threshold range can be removed. After that, a collinearity analysis of the remaining features was carried out by using the Pearson correlation coefficient, because even

though features play an important role in classification, there will still be cases where some features are strongly related.

2.3.4. Convolutional Neural Network (CNN)

A CNN is a multilayer feedforward neural network specifically intended for handle large-scale image or sensory data in the multiple arrays formation by taking global and local stationary characteristics into consideration [45]. The main components of a CNN usually consist of multiple layers interconnected with each other via a group of learnable weights and biases [46]. Each layer is filled with small patches of images that survey the entire image to acquire distinct local and global scale features. These image patches are generalized by other convolutional layers and pooling/sub-sampling layers within the CNN framework until advanced features are obtained and fully connected and classified [47]. In addition, there may be several feature maps after each convolution, and convolution kernels weights in the same feature map are shared. With this setting, the network can learn different functions while keeping the parameters number controllable. In addition, non-linear activations (such as sigmoid, hyperbolic tangent, linear element correction) functions were utilized outside the convolutional layer to enhance non-linearity [48]. In this paper, the Keras library in the Python language was applied to develop the CNN algorithm [49].

2.3.5. Support Vector Machine (SVM)

SVM is a multi-variable non-linear machine learning method with advantages of quick training converge, high training efficiency and good generalization performance [50]. SVMs are mainly constructed based on the structured risk minimization principle and statistical learning theory. Generally, the input variables are mapped from a relatively low feature space to a higher-dimensional feature space through the kernel function of the SVM model to solve the problems of linear inseparability and data dimension calculation. The radial basis function (RBF) is selected as the kernel function of the SVM in this study, because of its high efficiency of nonlinear mapping [10]. Besides the selection of the kernel function, two other parameters need to be set appropriately in the SVM; the penalty term C and the kernel function parameter gamma. A cross-validation stage method, which was proposed by [51], is recommended for the optimal combination of these three parameters. In this paper, the Sklearn library in Python language was used to develop the SVM algorithm [52].

2.3.6. Accuracy Assessment

To assess the performance of the proposed CNN-based OMM (CNNOMM) method, four standard evaluation metrics based on the confusion matrix are used. These evaluation metrics are overall accuracy (*OA*), Kappa coefficient (*KC*), producer accuracy (*PA*), and user accuracy (*UA*), and the values of these evaluation metrics were compared with that of SVM. *OA* indicates the overall performance of the models. *KC* was used to evaluate the reliability of the models. *PA* shows how often real ground samples are correctly shown on the classified map while *UA* indicates how often the class on the map will actually be present on the ground. Moreover, the McNemar's test is also used to test whether there is a statistical significant difference between the CNNOMM method and the SVM-based OMM method. The McNemar's test is a renowned statistical test for testing if the proportions of two dichotomous variables are equal [53].

3. Results

3.1. Results of Image Segmentation

The trial-and-error method is used to find the suitable CP, ShP, smoothness, and compactness parameters for the implementation of MSS using eCognition® software. In order to keep the segmented image objects representing the contour information of a target ground object, the CP, ShP, smoothness, and compactness values were set to 0.9, 0.1, 0.5 and 0.5, respectively (Table 2).

Table 2. Parameters utilized in multi-scale segmentation (MSS). ScP: scale parameter; CP: color parameter; ShP: shape parameter; OM: open-pit mine; WDA: waste-dump area; BUI: buildings; VEG: vegetation; ROA: road; WAT: water; BAS: bare soil.

Segmentation Level	Objects	ScP	CP/ShP	Smoothness/Compactness
Level-1	BUI, ROA	50	0.7/0.3	0.5/0.5
Level-2	OM, WDA	90	0.7/0.3	0.5/0.5
Level-3	WAT, VEG, BAS	120	0.7/0.3	0.5/0.5

The optimal ScP parameter of each LUC was determined by using the MAR method. The map of MAR values vary with the ScP was shown in Figure 4.
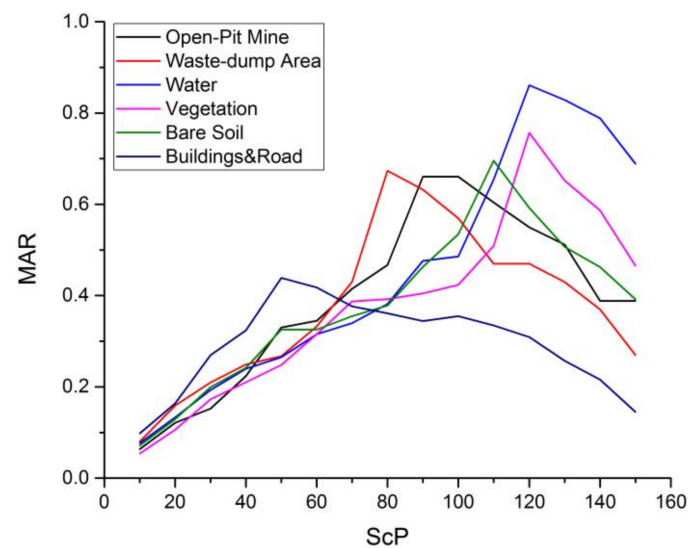
Figure 4. Map of mean area ratio (MAR) values vary with the Scale parameter (ScP).

Figure 4 indicates that the optimal ScP values of the seven LUCs are almost different, but they are clustered around three values, which are 120 of ScP value (WAT, VEG, and BAS), 90 of ScP value for OM and WDA, and 50 for the BUI and ROA. These seven LUCs can be segmented in three different levels, and the parameters used in the image segmentation are shown in Table 2.

Then, the GF-2 image of the study area was segmented into 48,277 objects by using eCognition® software. Finally, a sample set with 8326 sample objects was created based on the centroid inclusion principle by combing the segmented objects with the existing OMs and land use vectors. All the sample objects were divided into two parts in the ratio of 2:1, one is TTS, and the remaining is VS. The TTS is used to train and test the model, while the VS is used to validate the results. Then, the sample objects in TTS were split into two groups; training set and testing set, at the ration of 7:3. The details of sample set are listed in Table 3.

Table 3. Sample set utilized in this study. LUCs: land use categories.

LUCs	Training Set	Test Set	Validation Set	Sum
OM	731	313	522	1566
WDA	654	280	467	1401
BUI	601	258	429	1288
VEG	698	299	499	1496
ROA	542	232	387	1161
WAT	120	51	86	257
BAS	540	231	386	1157
total	3886	1664	2776	8326

3.2. Results of Feature Selection

The importance value was set as the average value of the 10 times training of GBDT to reduce the random error. Since there is no universal guideline for determining the threshold of cumulative importance value without a trial-and-error method, we set the threshold to set to 0.99 after several trial-and-error attempts to keep the most important features. Features that do not contribute to achieving 99% total importance value were eliminated. Figure 5 shows the overall cumulative importance curve. From Figure 4, we can see that 51 out of all 58 features have a cumulative importance of 99%. The cumulative importance of the remaining seven features is only 1%, which can be eliminated. These seven eliminated features are *Brightness*, $GLCM_{\text{all dir.}}$ (Dissimilarity), $GLCM_{\text{all dir.}}$ (Entropy), $GLCM_{\text{all dir.}}$ (Contrast), $GLCM_{\text{all dir.}}$ (Mean), Border index, and Elliptic fit.
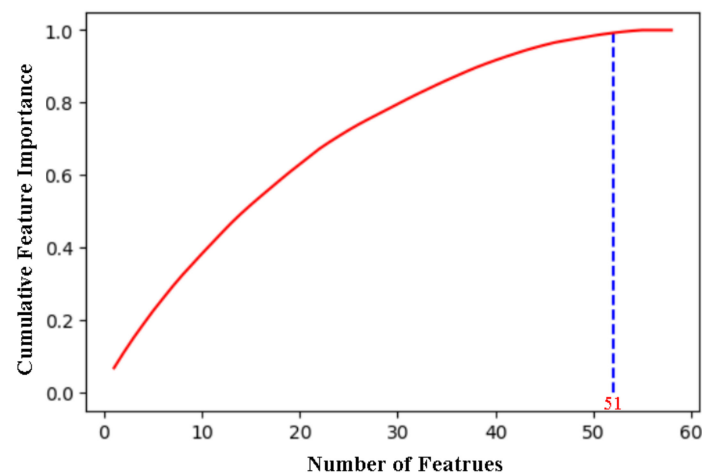
Figure 5. Overall cumulative importance curve.

After the elimination of the least important features, the collinearity among the 51 remaining features was analyzed by using the Pearson correlation coefficient. Then, the feature pair whose correlation absolute value is greater than the threshold value was selected, and one feature from the feature pair was removed. The trial-and-error method was also used to determine the threshold value of the Pearson correlation coefficient, which was set to 0.98 in this study to avoid eliminating too many features, and five features were removed. The thermodynamic chart of these 51 features and eliminated five features are shown in Figures 6 and 7. The five eliminated features are Mean_2, Ratio_2, Ratio vegetation index, and Mean Diff. to Neighbors_(1,3). In total, the features employed in the final OMM were decreased from 58 to 46 (see Table 4).

Table 4. Selected features employed in this study.

| OFDs (No.)	Features Names
LFs (26)	*Stdv*_(1,2,3,4), *Mean*_(1,3,4), *Ratio*_(1,3,4), *MaxDiff*, Shadow vegetation index, Normalized difference vegetation index, Normalized difference water index, Soil brightness index, Soil adjust vegetation index, Mean Diff. to Neighbors_(2,4), Mean Diff. to brighter Neighbors_(1,2,3,4), Mean Diff. to darker Neighbors_(1,2,3,4)
TFs (8)	$GLCM_{\text{all dir.}}$ (Angular second moment, Entropy, Stdv, Contrast, Homogeneity, Mean, Correlation) $GLDV_{\text{all dir.}}$ (Angular second moment)
GFs (12)	Area, Border length, Length, Width, Length-width ratio, Shape index, Roundness, Rectangular fit, Compactness, Main direction, Asymmetry, Density
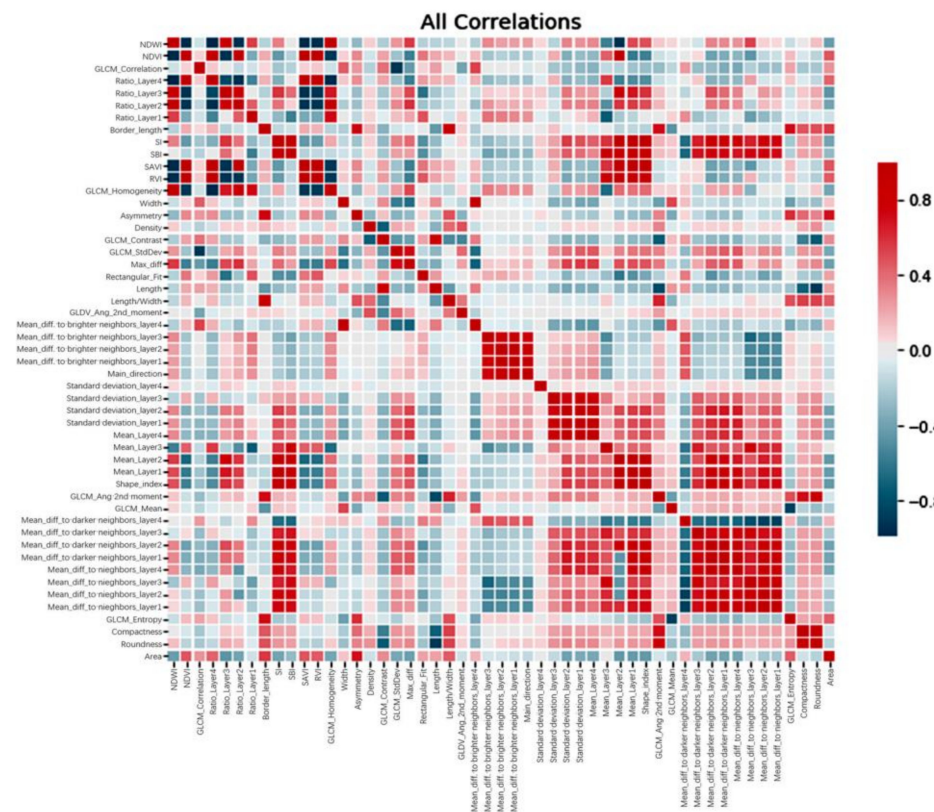
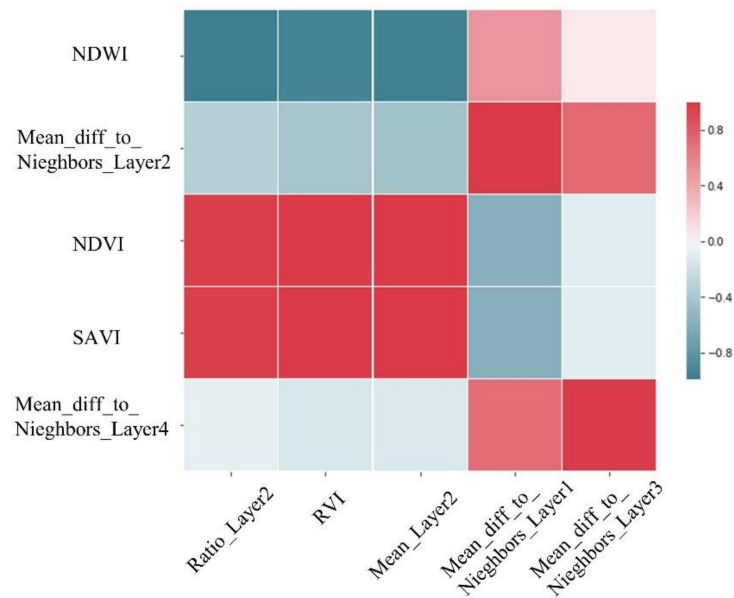**Figure 6.** Thermodynamic chart of the remaining 51 features.

Figure 7. Thermodynamic chart of the five eliminated features.

3.3. Results of Open-Pit Mine Mapping

3.3.1. CNN-Based Open-Pit Mine Mapping (CNNOMM)

A CNN network structure, including two convolutional layers, two pooling layers, two fully connected layers, and one dropout layer, is constructed by using the sequential model in Keras.

The form of convolution uses one-dimensional convolution, and the network structure is shown in Figure 8.
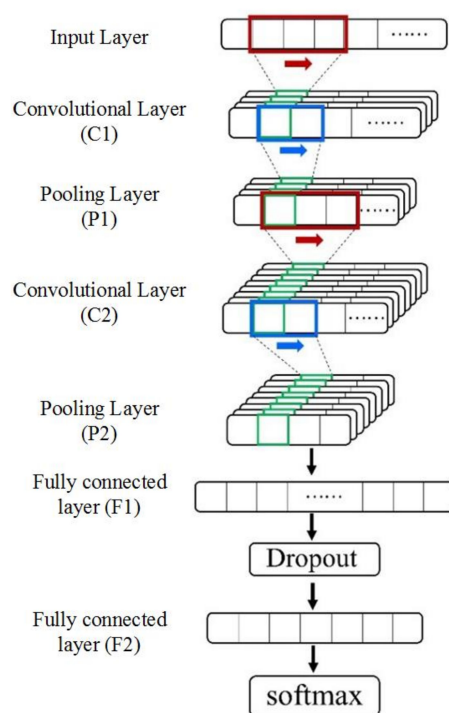
Figure 8. The network structure of CNN used in this study.

The number of convolution kernels (CKs) of the convolution layer C1 and C2 is set to 32 and 64, respectively, after several trial-and-error attempts. The size of CKs in C1 is set to 6×1, and the step size is set to 1, while the CKs in C2 is set to 3×1, and the step size is set to 1. The pooling layer P1 and P2 adopts the maximum pooling method to perform feature compression and extract retained features. The size of the P1 and P2 both are 2×1, and the step size for both are 2. The result of convolution and pooling is flattened and linearly mapped to the new feature space through the fully connected layer F1. The parameter of the Dropout layer is set to 0.5, which means that the connection between all the nods will be randomly cut off by 50%. There are seven neurons in the Fully connected layer F2 corresponding to the seven LUCs in this study, which are connected to the softmax classifier to achieve classification and serve as the output layer.

After the CNN is constructed, the TTS is employed to train the model and verify the learning effect. The Cross-Entropy Loss function [54] is selected to judge the differences between the predicted result and the reference value, while the Adam was applied as the optimization function. Figure 9 shows the Convergence curves of TTS of CNN.

From Figure 9 we can see that when the epoch reached the 35th time the accuracy of the test samples of the model finally reaches an accuracy of 0.89. At the same time, the loss rate of the test samples also tends to be stable. Then, the well-trained CNN was applied into the total 48,227 objects, Figure 10 shows the CNN-based OMM results.

The red color area in the figure is the OM extracted by the CNN-based open-pit mine mapping model. The black dashed area shows the verified open-pit mine. In Figure 8 we can see that the extracted OM results are in good agreement with the verified OM. However, there are still some OMs that are not identified by the proposed CNN-based open-pit mine mapping model, which are misclassified to WDA. Further discussion will be presented in Section 4.1.
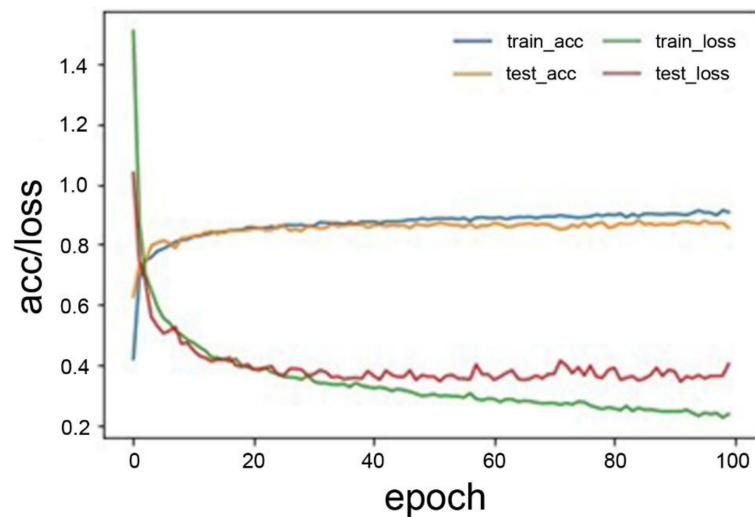
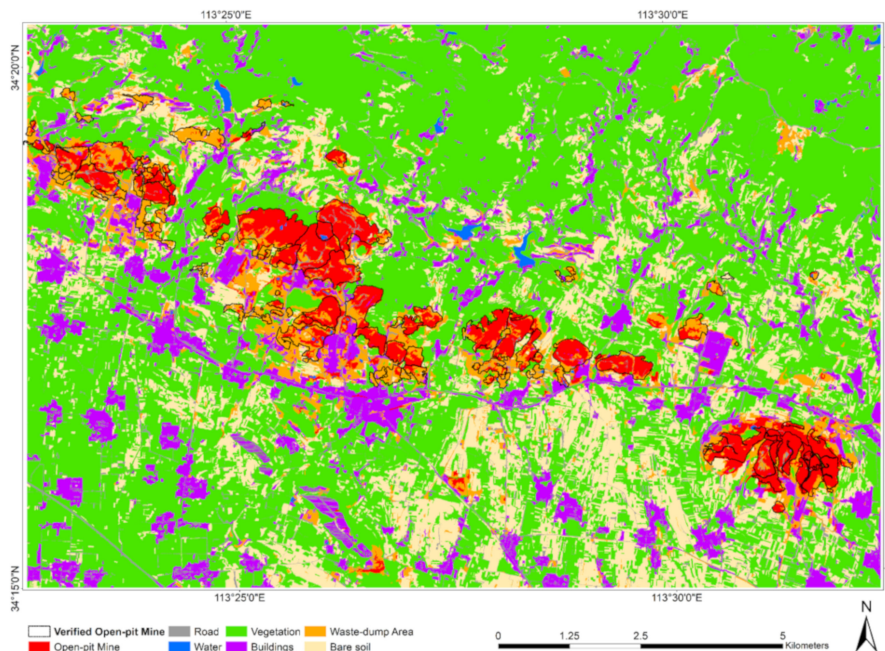**Figure 9.** Convergence curves of accuracy and loss of CNN based on training and testing set.

Figure 10. Results of CNN-based open-pit mine mapping.

3.3.2. SVM-Based Open-Pit Mine Mapping (SVMOMM)

We used the same TTS as we used in CNN model, to train and validate the SVM model. Then, the 10-fold cross-validation method [50] was applied to identify the appropriate SVM model parameters. It is suggested that the cost constant C and the kernel function parameter gamma are set to 10 and 0.045, respectively. Finally, the SVM-based OMM results are obtained (Figure 11).

Figure 11 shows nearly the same performance as Figure 8, which means the SVMOMM model can also achieve satisfied results. However, the omission phenomenon (misclassified OM into WDA) still exists and is more serious than CNNOMM model. We discuss this further in Section 4.1.
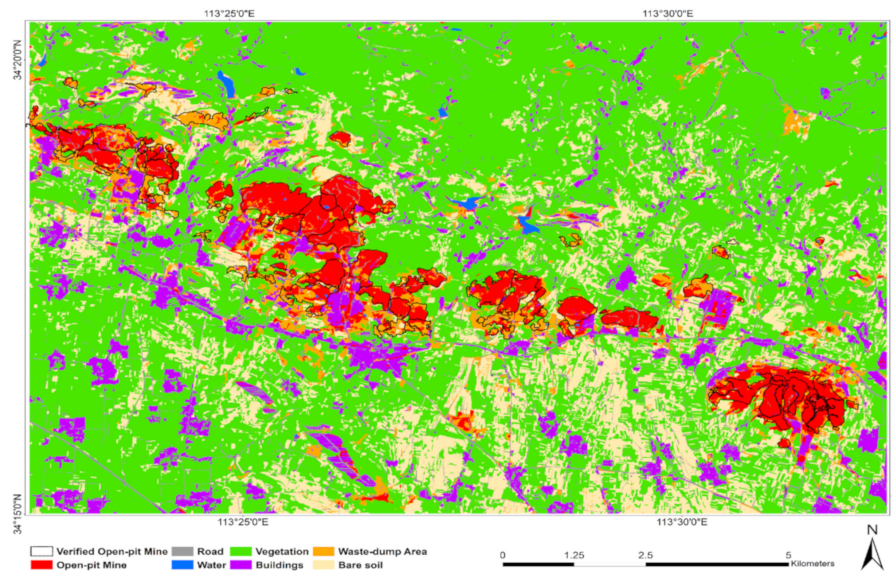
Figure 11. Results of SVM-based open-pit mine mapping.

3.3.3. Assessment of Mapping Results

The assessment of OMM results are based on VS. The confusion matrix and the accuracy assessment of these two methods are listed in Tables 5 and 6, respectively.

Table 5. Confusion matrix of OMM results of CNN/SVM.

LUCs	OM	WDA	BUI	VEG	ROA	WAT	BAS	Sum
OM	466/439	6/5	0/2	2/4	11/13	29/43	8/16	522/522
WDA	5/5	361/355	0/0	2/3	10/14	2/5	7/5	387/387
BUI	1/3	0/0	81/77	2/3	1/2	1/1	0/0	86/86
VEG	7/15	3/4	1/0	455/421	8/13	15/21	10/25	499/499
ROA	10/12	16/28	2/2	2/2	393/368	4/11	2/6	429/429
WAT	37/59	10/17	1/3	7/11	15/19	391/349	6/9	467/467
BAS	11/20	0/3	0/0	7/7	0/2	13/31	355/323	386/386
Sum	537/553	396/412	85/84	477/451	438/431	455/461	388/384	2776/2776

Table 6. Accuracy assessment of OMM results of CNN/SVM.

LUCs	Total Samples	Mapped Samples	Correct Samples	*UA* (%)	*PA* (%)
OM	522/522	537/553	466/439	86.78/79.39	89.27/84.10
WDA	387/387	396/412	361/355	91.16/86.17	93.28/91.73
BUI	86/86	85/84	81/77	95.29/91.67	94.19/89.53
VEG	499/499	477/451	455/421	95.39/93.35	91.18/84.37
ROA	429/429	438/431	393/368	89.73/85.38	91.61/85.78
WAT	467/467	455/461	391/349	85.93/75.70	83.73/74.73
BAS	386/386	388/384	355/323	91.49/84.11	91.97/83.68
OA (%)			90.13/84.01		
KC			0.88/0.81		

In general, CNNOMM was more effective in classifying all the seven LUCs, with higher *PA* and *UA* values, which means the CNNOMM mapped a greater number of correct samples than that of the SVMOMM classified. Among these seven LUCs, the *PA* values are higher than *UA* values in OM, WDA, ROA, both in CNNOMM and SVMOMM, and a higher *PA* in BAS in CNNOMM but a lower *PA* in SVMOMM. For the other three LUCs, which are BUI, VEG, and WAT, both two methods obtained

a high *UA*. A higher *PA* means that more objects were misclassified into other LUCs, and a higher *UA* means the number of mapped samples were less than that of total samples.

Figures 12 and 13 shows the incorrect mapping results of CNNOMM and SVMOMM, respectively. The incorrect mapping results shown in Figures 12 and 13 are consistent with that shown in Table 6, as most of the wrongly mapped LUCs are around the mining area. Figure 14 shows the results of the incorrect identification of CNNOMM and SVMOMM together. The yellow color represents the LUC, which is incorrectly mapped by both CNNOMM and SVMOMM. Most of them were WAT or OM LUC category, which indicates that these two LUC categories are easily misclassified between each other; the main reason is discussed in Section 4.1.
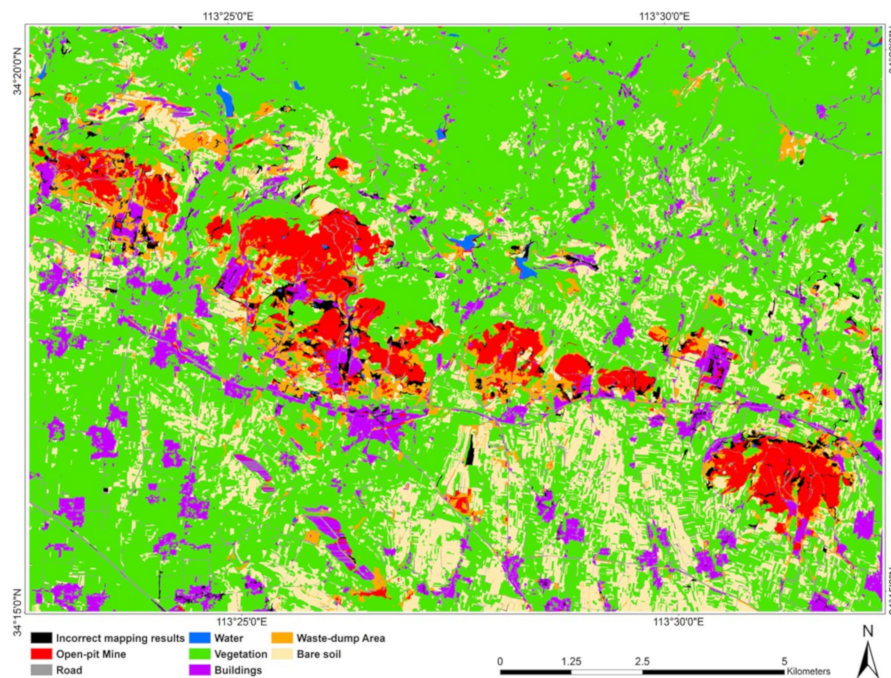
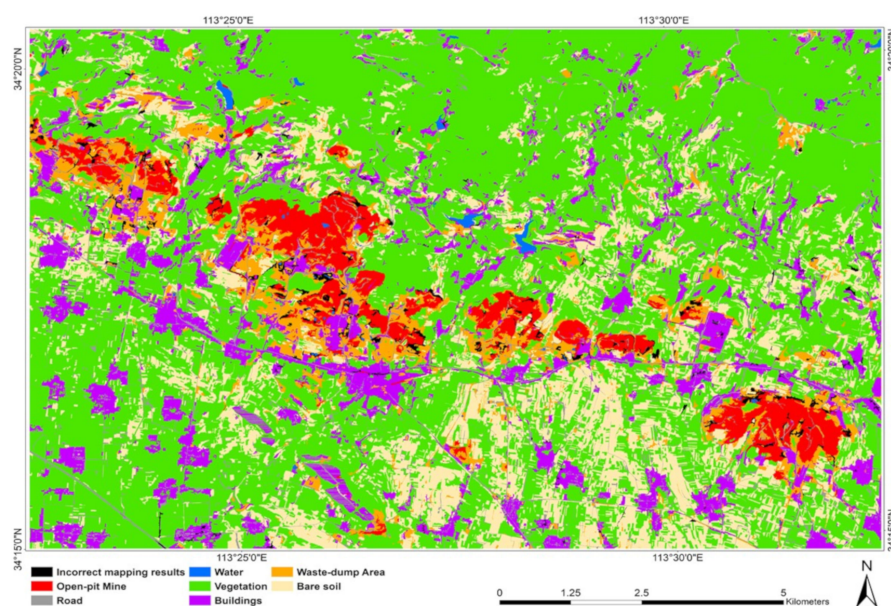**Figure 12.** Results of LUCs identification and incorrect identifications of CNNOMM.

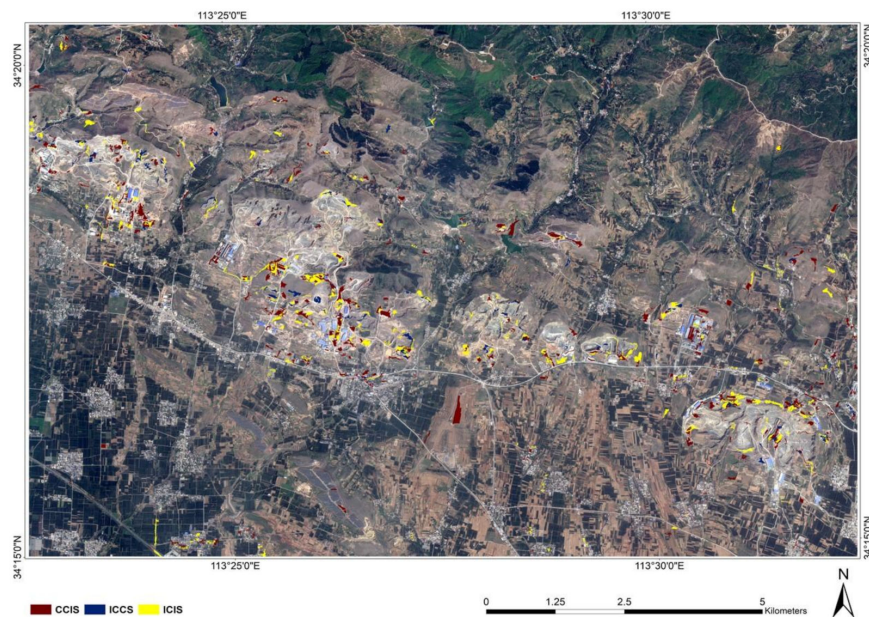**Figure 13.** Results of LUCs identification and incorrect identifications of SVMOMM.

Figure 14. Results of incorrect identifications of CNNOMM and SVMOMM. CCIS: correct mapping results of CNNOMM while incorrectly mapped by SVMOMM; ICCS: incorrect mapping results of CNNOMM while correctly mapped by SVMOMM; ICIS: incorrect mapping results both by CNNOMM and SVMOMM.

3.3.4. McNemar's Test

The McNemar's test is performed on the pair of CNNOMM and SVMOMM models. Table 7 shows the paired classification models, the number of objects correctly classified by one model but misclassified by another model, as well as the corresponding chi-square value and *p*-value.

Table 7. McNemar's test results for OMM. fij: the numbers of objects that were correctly classified by classifier i but misclassified by j (i, j = 1, 2); χ2: chi-square; ρ: probability value.

Pair of Classifications	f12	f21	χ2	ρ
CNNOMM vs. SVMOMM	458	262	53.36	<0.0001

It can be concluded that: (1) the CNNOMM significantly outperformed SVMOMM based on the chi-square value, which was larger than 3.84 and the *p* values smaller than 0.05. It is indicated that the mapping performance of the CNNOMM method is significantly improved; (2) CNNOMM and SVMOMM are significantly different.

4. Discussion

4.1. Affecting Factors of Mapping Accuracy

It is significant that CNNOMM improve the mapping accuracy of all the seven LUCs of the open-pit mine area. The accuracy of the five LUCs for non-mining activities such as WAT, VEG, BUI, BAS, and ROA is generally higher than the overall accuracy. The main reason is that these five types of features are common objects of land use types, and their image features, texture features, etc., are more obvious, which is easy to distinguish. There are certain similarities in the land use types which are caused by mining activities (OM and WDA). Sometimes these two LUCs are not easily distinguished because the materials which formed the WDA are extracted from the OM. There are differences caused by the influence of the topography, landforms, and human activities within these two LUCs. This also reflects the difficulty and importance of mining information extraction from one aspect.

There are some misclassifications between OM and WDA. There are two main reasons for these phenomena: one is that the OM and WDA are closely related in the process of their formation. The waste gravel piles and dumps in the OM and WDA are all formed with the formation of the OM. There are natural similarities in spectrum and texture. Another reason is that, as the country vigorously manages the mining environment in recent years, a large number of OMs have been shut down and governed. The lack of human mining activities may result in muck piles of rocks inside the pits. This part of the OM darkens in the spectrum, and the texture begins to appear patchy, which will appear similar to the mine wastes over time, which is easy to be confused (Figure 15). Figure 15b shows the mapping results of CNNOMM. From Figure 15a, it is hard to accurately determine its type by visual interpretation. According to the field validation of the mapping results in 2018, it can be determined that the area is an open pit and has been abandoned for many years, resulting in confusion in type.
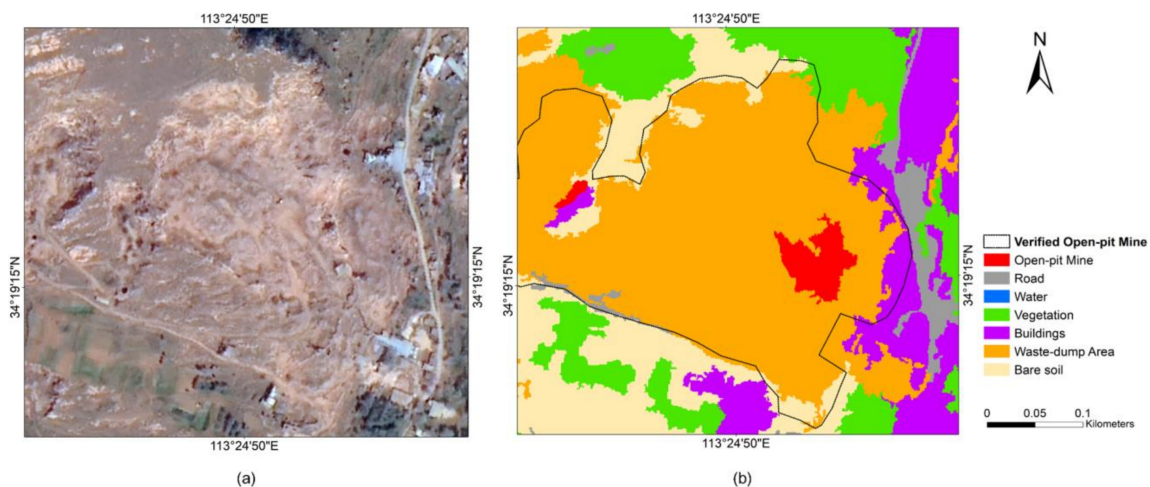

Figure 15. Abandoned OM in the study area. (**a**) GF-2 image; (**b**) CNNOMM results.

4.2. Uncertainties in OMM

Although the CNNOMM model achieves reasonable and promising results in the study area, there are still some uncertainties. Firstly, in the image segmentation progress, uncertainties will be introduced in OMM, because the OMs and land use references cannot be subdivided into exact objects. Although the MAR method can optimize the scale values, which improves the segmentation results, errors are inevitable and will cause a decrease in the OMM accuracy [21]. Secondly, uncertainties may be introduced in the process of selecting features, because the importance of such features with the two methods is not the same. These will also decrease the mapping accuracy of OM, even though their importance can be calculated [22]. Last but not the least, the complete and consistent OM inventory in the study area were insufficient. This insufficiency may also lead to uncertainties, because some newly OM in the research area may not have been recognized in the existing OM inventory datasets.

5. Conclusions

In this paper, we proposed a hybrid framework of object-oriented open-pit mine mapping to classify the open-pit mines in Yuzhou City from 'GF-2' HSRSIs. The framework utilizes the greater generalization performance of CNN and the effective elimination of redundant features by a FIR tool.

In total, 58 features were extracted from GF-2 HSRSI from three object-feature domains. By using the FIR tools, which were GBDT and Pearson correlation coefficient, 46 features were selected to form the features subset. The final mapping results demonstrate that the proposed FIR tools can provide valid information for OOMM.

A sample set with 8326 sample objects was created by combing the segmented objects with the existing OMs and land use vectors based on a centroid inclusion principle method. Two thirds of

the sample set formed the TTS, while the remaining one third was used as VS. The TTS (combined with the features subset) were used to train and test the CNN and SVM model, and the *OA*, and *KC* of the remaining VS were found to be 90.13%, and 0.88 for CNN, 84.01% and 0.81 for SVM, respectively. It indicated that the CNN outperformed the SVM in the proposed OOMM framework. Thus, it can be concluded that, based on the features obtained from 'GF-2' HSRSI, our feature information reduction method (combined with CNN) can provide an effective way for OOMM in Yuzhou City.

Author Contributions: Conceptualization, T.C.; methodology, N.H.; software, N.H.; validation, T.C., N.H. and N.Z.; formal analysis, T.C., N.H. and A.P.; investigation, T.C.; resources, T.C. and R.N.; data curation, N.H.; writing—original draft preparation, N.H. and T.C.; writing—review and editing, R.N. and A.P.; supervision, T.C. All authors have read and agreed to the published version of the manuscript.

Conflicts of Interest: The authors declare no conflict of interest.

References

1. Braghină, C.; Peptenatu, D.; Constantinescu, Ș.; Pintilii, R.D.; Drăghici, C. The pressure exerted on the natural environment in the open pit exploitation areas in Oltenia. *Carpath. J. Earth Environ. Sci.* **2010**, *5*, 33–40.

2. Fytas, K.; Paraszczak, J. Satellite Remote Sensing as Means to Assess Primary Impact of Open-Pit Mining Development. In *International Mining Forum 2006, New Technological Solutions in Underground Mining: Proceedings of the 7th International Mining Forum, Cracow-Szczyrk-Wieliczka, Poland, February 2006*; CRC Press: Boca Raton, FL, USA, 2006; p. 161.

3. Sengupta, S.; Krishna, A.P.; Roy, I. Slope failure susceptibility zonation using integrated remote sensing and GIS techniques: A case study over Jhingurdah open pit coal mine, Singrauli coalfield, India. *J. Earth Syst. Sci.* **2018**, *127*, 82. [CrossRef]

4. Francioni, M.; Salvini, R.; Stead, D.; Giovannini, R.; Riccucci, S.; Vanneschi, C.; Gullì, D. An integrated remote sensing-GIS approach for the analysis of an open pit in the Carrara marble district, Italy: Slope stability assessment through kinematic and numerical methods. *Comput. Geotech.* **2015**, *67*, 46–63. [CrossRef]

5. Ozdogan, M.V.; Deliormanli, A.H. Monitoring of landslide at Tuncbilek open pit stripping area with terrestrial laser scanner and optical images. *IOP Conf. Ser. Earth Environ. Sci.* **2016**, *44*, 042035. [CrossRef]

6. Chen, W.T.; Li, X.J.; He, H.X.; Wang, L.Z. A Review of Fine-Scale Land Use and Land Cover Classification in Open-Pit Mining Areas by Remote Sensing Techniques. *Remote Sens.* **2018**, *10*, 15. [CrossRef]

7. Yu, L.; Xu, Y.; Xue, Y.; Li, X.; Cheng, Y.; Liu, X.; Porwal, A.; Holden, E.J.; Yang, J.; Gong, P. Monitoring surface mining belts using multiple remote sensing datasets: A global perspective. *Ore Geol. Rev.* **2018**, *101*, 675–687. [CrossRef]

8. Maxwell, A.E.; Warner, T.A.; Strager, M.P.; Pal, M. Combining Rapid Eye Satellite Imagery and Lidar for Mapping of Mining and Mine Reclamation. *Photogramm. Eng. Remote Sens.* **2014**, *80*, 179–189. [CrossRef]

9. Maxwell, A.E.; Warner, T.A.; Strager, M.P.; Conley, J.F.; Sharp, A.L. Assessing machine-learning algorithms and image- and lidar-derived variables for GEOBIA classification of mining and mine reclamation. *Int. J. Remote Sens.* **2015**, *36*, 954–978. [CrossRef]

10. Chen, W.T.; Li, X.J.; Wang, L.Z. Fine Land Cover Classification in an Open Pit Mining Area Using Optimized Support Vector Machine and WorldView-3 Imagery. *Remote Sens.* **2020**, *12*, 82. [CrossRef]

11. Peng, Y.; Zhang, Z.M.; He, G.J.; Wei, M.Y. An Improved GrabCut Method Based on a Visual Attention Model for Rare-Earth Ore Mining Area Recognition with High-Resolution Remote Sensing Images. *Remote Sens.* **2019**, *11*, 987. [CrossRef]

12. Goldblatt, R.; You, W.; Hanson, G.; Khandelwal, A.K. Detecting the Boundaries of Urban Areas in India: A Dataset for Pixel-Based Image Classification in Google Earth Engine. *Remote Sens.* **2016**, *8*, 634. [CrossRef]

13. Mountrakis, G.; Im, J.; Ogole, C. Support vector machines in remote sensing: A review. *ISPRS J. Photogramm. Remote Sens.* **2011**, *66*, 247–259. [CrossRef]

14. Schalko, R.J. *Artificial Neural Networks*; McGraw-Hill Higher Education: New York, NY, USA, 1997.

15. Lobo, F.D.; Souza, P.W.M.; Novo, E.; Carlos, F.M.; Barbosa, C.C.F. Mapping Mining Areas in the Brazilian Amazon Using MSI/Sentinel-2 Imagery (2017). *Remote Sens.* **2018**, *10*, 1178. [CrossRef]

16. Blaschke, T. Object based image analysis for remote sensing. *ISPRS J. Photogramm. Remote Sens.* **2010**, *65*, 2–16. [CrossRef]

17. Zhang, Z.M.; He, G.J.; Wang, M.M.; Wang, Z.H.; Long, T.F.; Peng, Y. Detecting Decadal Land Cover Changes in Mining Regions based on Satellit Remotely Sensed Imagery: A Case Study of the Stone Mining Area in Luoyuan County, SE China. *Photogramm. Eng. Remote Sens.* **2015**, *81*, 745–751. [CrossRef]

18. Song, X.L.; He, G.J.; Zhang, Z.M.; Long, T.F.; Peng, Y.; Wang, Z.H. Visual attention model based mining area recognition on massive high-resolution remote sensing images. *Cluster Comput.* **2015**, *18*, 541–548. [CrossRef]

19. Zhang, M.L.; Zhou, W.; Yuan, T.; Xie, Y.H.; Li, Y.F. Object-based change monitoring in mining areas-taking Pingshuo as an example. In *Land Reclamation in Ecological Fragile Areas*; CRC Press-Balkema: Leiden, The Netherlands, 2017; pp. 127–130.

20. Chen, L.; Li, W.; Zhang, X.; Chen, L.; Chen, C. Application of Object-oriented Classification with Hierarchical Multi-Scale Segmentation for Information Extraction in Nonoc Nickel Mine, the Philippines. In *Proceedings of the 2018 Fifth International Workshop on Earth Observation and Remote Sensing Applications Xi'an, China 18–20 June 2018*; Weng, Q., Gamba, P., Chang, N.B., Wang, G., Yao, W., Eds.; IEEE: New York, NY, USA, 2018; pp. 378–380.

21. Chen, T.; Trinder, J.C.; Niu, R.Q. Object-Oriented Landslide Mapping Using ZY-3 Satellite Imagery, Random Forest and Mathematical Morphology, for the Three-Gorges Reservoir, China. *Remote Sens.* **2017**, *9*, 333. [CrossRef]

22. Chen, Y.S.; Jiang, H.L.; Li, C.Y.; Jia, X.P.; Ghamisi, P. Deep Feature Extraction and Classification of Hyperspectral Images Based on Convolutional Neural Networks. *IEEE Trans. Geosci. Remote Sens.* **2016**, *54*, 6232–6251. [CrossRef]

23. LeCun, Y.; Kavukcuoglu, K.; Farabet, C. Convolutional Networks and Applications in Vision. In Proceedings of the 2010 IEEE International Symposium on Circuits and Systems, Paris, France, 30 May–2 June 2010; pp. 253–256.

24. Krizhevsky, A.; Sutskever, I.; Hinton, G.E. ImageNet Classification with Deep Convolutional Neural Networks. *Commun. ACM* **2017**, *60*, 84–90. [CrossRef]

25. Othmana, E.; Bazi, Y.; Alajlan, N.; Alhichri, H.; Melgani, F. Using convolutional features and a sparse autoencoder for land-use scene classification. *Int. J. Remote Sens.* **2016**, *37*, 2149–2167. [CrossRef]

26. Chen, X.Y.; Xiang, S.M.; Liu, C.L.; Pan, C.H. Vehicle Detection in Satellite Images by Hybrid Deep Convolutional Neural Networks. *IEEE Geosci. Remote Sens. Lett.* **2014**, *11*, 1797–1801. [CrossRef]

27. Dong, Z.; Pei, M.; He, Y.; Liu, T.; Dong, Y.; Jia, Y. Vehicle Type Classification Using Unsupervised Convolutional Neural Network. In Proceedings of the 2014 22nd International Conference on Pattern Recognition, Stockholm, Sweden, 24–28 August 2014; pp. 172–177.

28. Cheng, G.L.; Wang, Y.; Xu, S.B.; Wang, H.Z.; Xiang, S.M.; Pan, C.H. Automatic Road Detection and Centerline Extraction via Cascaded End-to-End Convolutional Neural Network. *IEEE Trans. Geosci. Remote Sens.* **2017**, *55*, 3322–3337. [CrossRef]

29. Sargent, I.; Hare, J.; Young, D.; Wilson, O.; Doidge, C.; Holland, D.; Atkinson, P.M. Inference and Discovery in Remote Sensing Data with Features Extracted Using Deep Networks. In *Artificial Intelligence XXXIV, SGAI 2017 Lecture Notes in Artificial, Intelligence*; Bramer, M., Petridis, M., Eds.; Springer International Publishing Ag: Cham, The Netherlands, 2017; Volume 10630, pp. 131–136.

30. Zhao, W.Z.; Du, S.H.; Wang, Q.; Emery, W.J. Contextually guided very-high-resolution imagery classification with semantic segments. *ISPRS J. Photogramm. Remote Sens.* **2017**, *132*, 48–60. [CrossRef]

31. Duro, D.C.; Franklin, S.E.; Dube, M.G. Multi-scale object-based image analysis and feature selection of multi-sensor earth observation imagery using random forests. *Int. J. Remote Sens.* **2012**, *33*, 4502–4526. [CrossRef]

32. Baatz, M.; Schäpe, A. Multiresolution Segmentation: An optimization approach for high quality multi-scale image segmentation. In *Angewandte Geographische, Informationsverarbeitung XII. Beitrge zum AGIT-Symposium, 2000*; Strobl, J., Blaschke, T., Griesebner, G., Eds.; Wichmann-Verlag: Heidelberg, Germany, 2000; pp. 12–23.

33. Laliberte, A.S.; Rango, A.; Herrick, J.E.; Fredrickson, E.L.; Burkett, L. An object-based image analysis approach for determining fractional cover of senescent and green vegetation with digital plot photography. *J. Arid Environ.* **2007**, *69*, 1–14. [CrossRef]

34. Sandric, I.; Mihai, B.; Chitu, Z.; Gutu, A.; Savulescu, I. Object-oriented methods for landslides detection using high resolution imagery, morphometric properties and meteorological data. In *Proceedings of the ISPRSTCVII Symposium Vienna, Austria 5–7 July 2010*; Wagner, W., Szekely, B., Eds.; ISPRS: Berlin, Germany, 2010; Volume XXXVIII, pp. 486–490.

35. Definiens Professional Earth (DPE). *Definiens Professional 5 User Guide*; Definiens AG: München, Germany, 2006; p. 249.

36. Martha, T.R.; Kerle, N.; Jetten, V.; van Westen, C.J.; Kumar, K.V. Characterising spectral, spatial and morphometric properties of landslides for semi-automatic detection using object-oriented methods. *Geomorphology* **2010**, *116*, 24–36. [CrossRef]

37. Stumpf, A.; Kerle, N. Object-oriented mapping of landslides using Random Forests. *Remote Sens. Environ.* **2011**, *115*, 2564–2577. [CrossRef]

38. Haralick, R.M.; Shanmugam, K.; Dinstein, I.H. Textural Features for Image Classification. *IEEE Trans. Syst. Man Cybern.* **1973**, *SMC-3*, 610–621. [CrossRef]

39. Trimble. *eCognition Developer 8.64.0 Reference Book*; Germany Trimble Documentation: München, Germany, 2011.

40. Kursa, M.B.; Rudnicki, W.R. Feature Selection with the Boruta Package. *J. Stat. Softw.* **2010**, *36*, 1–13. [CrossRef]

41. Kohavi, R.; John, G.H. Wrappers for feature subset selection. *Artif. Intell.* **1997**, *97*, 273–324. [CrossRef]

42. Park, J.; Moon, J.; Jung, S.; Hwang, E. Multistep-Ahead Solar Radiation Forecasting Scheme Based on the Light Gradient Boosting Machine: A Case Study of Jeju Island. *Remote Sens.* **2020**, *12*, 2271. [CrossRef]

43. Tan, C.; Yan, W.; Tang, Q.; Wu, H.; Bu, H.; Kambi, S.J.; Liu, J. Casing Damage Prediction Model Based on the Data-Driven Method. *Math. Probl. Eng.* **2020**, *2020*, 8315908. [CrossRef]

44. Schapire, R.E. The Boosting Approach to Machine Learning: An Overview. In *Nonlinear Estimation and Classification*; Lecture Notes in Statistics; Denison, D.D., Hansen, M.H., Holmes, C.C., Mallick, B., Yu, B., Eds.; Springer: New York, NY, USA, 2003; Volume 171, pp. 149–171.

45. LeCun, Y.; Bengio, Y.; Hinton, G. Deep learning. *Nature* **2015**, *521*, 436–444. [CrossRef] [PubMed]

46. Romero, A.; Gatta, C.; Camps-Valls, G. Unsupervised Deep Feature Extraction for Remote Sensing Image Classification. *IEEE Trans. Geosci. Remote Sens.* **2016**, *54*, 1349–1362. [CrossRef]

47. Schmidhuber, J. Deep learning in neural networks: An overview. *Neural Netw.* **2015**, *61*, 85–117. [CrossRef] [PubMed]

48. Strigl, D.; Kofler, K.; Podlipnig, S. Performance and Scalability of GPU-based Convolutional Neural Networks. In *Proceedings of the 18th Euromicro Conference on Parallel, Distributed and Network-Based Processing, Pisa, Italy, 17–19 February 2010*; Danelutto, M., Bourgeois, J., Gross, T., Eds.; IEEE Computer Soc: Los Alamitos, CA, USA, 2010; pp. 317–324.

49. Developer Guides. Available online: https://keras.io/guides/ (accessed on 4 November 2020).

50. Cortes, C.; Vapnik, V. Support-Vector Networks. *Mach. Learn.* **1995**, *20*, 273–297. [CrossRef]

51. Huang, F.M.; Yin, K.L.; Huang, J.S.; Gui, L.; Wang, P. Landslide susceptibility mapping based on self-organizing-map network and extreme learning machine. *Eng. Geol.* **2017**, *223*, 11–22. [CrossRef]

52. User Guide. Available online: https://scikit-learn.org/stable/user_guide.html (accessed on 4 November 2020).

53. McNemar, Q. Note on the sampling error of the difference between correlated proportions or percentages. *Psychometrika* **1947**, *12*, 153–157. [CrossRef]

54. Miller, J.W.; Goodman, R.; Smyth, P. On loss functions which minimize to conditional expected values and posterior probabilities. *IEEE Trans. Inf. Theory* **1993**, *39*, 1404–1408. [CrossRef]